Biophysical Journal
Article

Biophysical Society

Engineering rhodopsins' activation spectra using a FRET-based approach

Connor Beck[1,*] and Yiyang Gong[1,*]
[1]Department of Biomedical Engineering, Duke University, Durham, North Carolina

ABSTRACT In the past decade, optogenetics has become a nearly ubiquitous tool in neuroscience because it enables researchers to manipulate neural activity with high temporal resolution and genetic specificity. Rational engineering of optogenetic tools has produced channelrhodopsins with a wide range of kinetics and photocurrent magnitude. Genome mining for previously unidentified species of rhodopsin has uncovered optogenetic tools with diverse spectral sensitivities. However, rational engineering of a rhodopsin has thus far been unable to re-engineer spectral sensitivity while preserving full photocurrent. Here, we developed and characterized ChroME-mTFP, a rhodopsin-fluorescent protein fusion that drives photocurrent through Förster resonance energy transfer (FRET). This FRET-opsin mechanism artificially broadened the activation spectrum of the blue-green-light-activated rhodopsin ChroME by approximately 50 nm, driving higher photocurrent at blue-shifted excitation wavelengths without sacrificing kinetics. The excitation spectra's increase at short wavelengths enabled us to optogenetically excite neurons at lower excitation powers with shorter wavelengths of light. Increasing this rhodopsin's sensitivity to shorter, bluer wavelengths pushes it toward dual-channel, crosstalk-free optogenetic stimulation and imaging with green-light-activated sensors. However, this iteration of FRET-opsin suffers from some imaging-light-induced photocurrent crosstalk from green or yellow light due to maintained, low-efficiency excitation at longer wavelengths.

SIGNIFICANCE Neuroscientists investigate relationships between genetically diverse ensembles of neurons. They aspire to dual-channel experiments that ascertain correlation and causation by either successively stimulating groups of neurons or stimulating one group and recording from another. Such experiments rely on spectrally separable optogenetic tools that stimulate neural activity with light. This work presents a first step toward manipulating the light wavelength sensitivity of optogenetic tools without directly engineering the rhodopsin's channel. By pairing a rhodopsin with the appropriate fluorescent protein FRET partner, we demonstrated a straightforward and potentially generalizable method to blue-shift a rhodopsin's excitation spectrum by 50 nm. This spectral broadening increased the spectral separation between our FRET-rhodopsin complex and green-light-sensitive protein tools, pushing them toward crosstalk-free, two-channel neuroscience experiments.

INTRODUCTION

Neuroscientists employ several classes of genetically encoded protein tools to study the neural circuits that encode information in the brain. One such class of tools is optogenetic actuators, including light-activated ion channels and pumps. These actuators enable researchers to exert precise control over neural circuits by exciting genetically defined populations of neurons with a range of light wavelengths (1–12). Optogenetic stimulation of subpopulations of individual neurons has recently been shown to influence behavior in awake animals (13–15). Advancing the ability to precisely control optogenetic stimulation of such subpopulations will enable the neuroscience field to perform refined perturbations of neural circuits with high temporal precision, high responsiveness, and accurate selectivity.

Recent engineering of various rhodopsins has resulted in a large suite of optogenetic tools that elicit a wide range of photocurrents with a wide range of on and off kinetics (8,11,12,16). Highly sensitive rhodopsins support robust activation of larger neural populations with low excitation powers and exposure times, while rapidly responsive rhodopsins support temporally precise neural activation. In addition to engineering photocurrent and speed, engineering a rhodopsin's excitation spectrum is also important: a rhodopsin's excitation spectrum dictates its applicability

Submitted October 19, 2021, and accepted for publication March 18, 2022.
*Correspondence: connor.beck@duke.edu or yiyang.gong@duke.edu
Editor: Vasanthi Jayaraman.
https://doi.org/10.1016/j.bpj.2022.03.024

in specific types of neuroscience experiments. Single-channel experiments that seek to perturb single populations of neurons may be better served by a green- or yellow-light-sensitive rhodopsin due to longer wavelengths' reduced scattering compared with blue light. Dual-channel experiments that seek to perturb or image multiple neural populations must employ two genetically encoded tools with mutually exclusive excitation wavelengths. One example experiment in this class is the simultaneous optogenetic stimulation of one genetically defined subset of neurons and imaging of activity from a second subset of neurons to determine how the first population influences the activity of the second. Such an experiment requires high spectral separation between each tool's excitation spectrum to minimize off-target excitation of rhodopsin-expressing neurons. To minimize this crosstalk, the excitation spectrum of the rhodopsin actuator should not overlap with the excitation spectrum of the genetically encoded indicator.

Rationally designed engineering of rhodopsin actuators has been only partially successful in supporting multichannel optical experiments, likely for two reasons. First, unlike modulations in sensitivity and kinetics that can often be achieved through targeted mutagenesis of key residues in a rhodopsin's sequence, modulating rhodopsins' activation spectra, or the range of wavelengths to which rhodopsins are sensitive, via directed evolution while maintaining their original sensitivity has not been straightforward (17–21). Instead, identifying or developing rhodopsins with novel excitation spectra has historically resulted from either genome mining for new rhodopsins (4,8,22,23) or by developing chimeric rhodopsins by fusing subunits of multiple rhodopsin species (4,6,8,24,25). Both of these methods require large scale in screening and characterization. Second, most pairings of highly sensitive rhodopsins and genetically encoded sensors suffer from varying levels of crosstalk due to incomplete separation of the rhodopsin's and sensor's excitation spectra. To achieve spectral separability between a sensor and actuator, researchers have often employed red-light-activated rhodopsins like C1V1 in conjunction with blue-light-sensitive indicators (26–28). However, this paradigm often results in inadvertent excitation of the rhodopsin by the imaging source due to the long tail of many rhodopsins' excitation spectra to the blue side of their peak activation wavelengths. For example, recently developed tools such as ChroME, a rhodopsin with enhanced two-photon photocurrent and kinetics developed through site-directed mutagenesis of the fast, cyan-light-activated rhodopsin Chronos, suffer from imaging-laser-induced photocurrent crosstalk upon direct excitation by 930-nm lasers used for two-photon imaging of green fluorescent sensors due to incomplete spectral separation (11). In the one-photon excitation domain, this crosstalk is even more pronounced. ChroME's one-photon excitation spectrum highly overlaps with GCaMP's; their peak excitation wavelengths are separated by only approximately 20 nm.

Alternatively, one could employ a blue-light-sensitive rhodopsin in conjunction with a yellow-light-activated red fluorescent sensor (29). This paradigm takes advantage of the sharp decrease in rhodopsins' excitation efficiency on the red edge of their activation spectra, minimizing off-target excitation of targeted neurons. ChroME is only somewhat compatible with red fluorescent sensors such as jRCaMP or jRGECO, but spectral overlap remains an issue: off-peak excitation of ChroME by one-photon 560-nm light used for imaging can still produce significant photocurrent.

In order to improve the spectral separability of optogenetic tools and genetically encoded sensors, it would be beneficial to develop rhodopsins with activation spectra blue-shifted from the state-of-the-art, high-sensitivity rhodopsins such as CoChR (8) and ChroME (11). Such a tool would ideally maintain the photocurrent sensitivity and fast kinetics of the parent rhodopsin while shifting its spectral sensitivity. In this work, we developed a rhodopsin construct that enhances the rhodopsin's response to shorter wavelengths through Förster resonance energy transfer (FRET) via fusion to a cyan fluorescent protein (CFP). This fusion facilitated excitation of the rhodopsin via FRET when the CFP was excited by blue light. Previous work has demonstrated fluorescent protein-rhodopsin interactions through both radiative and non-radiative excitation pathways. Fusing channelrhodopsins with luciferase demonstrated that radiative excitation of rhodopsins from nearby emitters could facilitate photocurrent (30,31). In contrast, non-radiative FRET has been employed in the development of genetically encoded voltage indicators (32–37) and FRET-assisted biosensors (38). Additionally, in a recent study characterizing a novel rhodopsin, an enhanced yellow fluorescent protein tag facilitated a red-light-activated rhodopsin's photocurrent (39). In this work, we build on this interaction and perform analyses that enable us to modulate the amplitude of this FRET effect for a cyan-light-activated rhodopsin. FRET enabled us to boost photocurrent and maintain fast kinetics at blue-shifted wavelengths relative to the rhodopsin's original activation spectrum. Rather than directly engineering the rhodopsins themselves, we instead rationally paired the protein with one of several engineered CFPs to enable high-FRET-efficiency excitation of the rhodopsin acceptor.

MATERIALS AND METHODS

Plasmid construction

We used overlap PCR to construct all plasmids including the mutation of Chronos to ChroME and fusion of either Rosmarinus (RSM) (40) or mTFP1 (41) to a truncated version of ChroME. We performed a second overlap PCR to fuse the targeting sequence (TS)-endoplasmic reticulum (ER) motif to the 3′ end of each construct to improve membrane localization. We expressed all constructs in a lentiviral backbone under the

CamkIIα promoter. ChroMEΔ15-mTFP is deposited on Addgene as plasmid #184240.

Cell culture

We cultured HEK293T cells in Dulbecco's modified Eagle's medium (DMEM) (Gibco, Waltham, MA) supplemented with 10% fetal bovine serum (FBS) (Gibco, Waltham, MA) and 1% penicillin-streptomycin (Gibco, Waltham, MA). We transfected cells using Lipofectamine 2000 (Thermo Fisher, Waltham, MA) 1 day after plating and imaged cells 2 days after transfection.

We cultured hippocampal neurons from P0 Sprague-Dawley rat pups (Charles River Labs, Chapel Hill, NC) and cultured them in Neurobasal Media A with B-27 (Gibco, Waltham, MA) and GlutaMAX (Gibco, Waltham, MA) cell culture supplements. We treated neuron cultures with fluorodeoxyuridine (FUDR) (Alfa Aesar, Ward Hill, MA) 2 days after plating to inhibit glial cell growth, transfected cells via calcium phosphate transfection 3 days after plating, and imaged neurons 6–9 days after plating.

Electrophysiology

We recorded the photocurrent of each construct in HEK293T cells and cultured rat hippocampal neurons using an Axon Digidata 1550A (Axon Instruments, San Jose, CA) digitizer, Multiclamp 700A amplifier (Axon Instruments, San Jose, CA), and pClamp software. We held HEK293T cells at a −65 mV holding potential in voltage clamp mode and recorded the photocurrent elicited by various wavelengths of light and pulse conditions. We held neurons in current clamp mode and injected current to maintain a −65-mV resting membrane potential. We performed a post hoc correction to account for the electrode's −10-mV junction potential.

We mounted all samples in a room temperature perfusion chamber. The extracellular media consisted of 150 mM NaCl, 4 mM KCl, 10 mM glucose, 10 mM HEPES, 2 mM $CaCl_2$, and 2 mM $MgCl_2$. The intracellular solution contained 129 mM K-gluconate, 10 mM KCl, 10 mM HEPES, and 4 mM Na_2ATP.

Optics

We used a 40×, 0.8 NA water immersion objective (CFI Apo NIR 40× W, MRD07420, Nikon, Melville, NY) for all imaging and photostimulation experiments. For the simultaneous calcium imaging, we used a scientific complementary metal-oxide-semiconductor (sCMOS) camera (OptiMOS, QImaging, Tuscon, AZ) and imaged cells at 25–50 Hz.

We used Thorlabs mounted light-emitting diodes (LEDs) to excite HEK293T cells for comparison of the peak photocurrent of each construct at 450 nm (M450LP1, Thorlabs, Newton, NJ) and 490 nm (M490L4, Thorlabs, Newton, NJ). The 490-nm LED passed through a 480/40-nm filter (ET480/40m, Chroma, Bellows Falls, VT); the 450-nm LED light passed through a 436/20-nm filter (ET436/20x, Chroma, Bellows Falls, VT) and joined the 490-nm excitation path after reflecting off a 455-nm long-pass dichroic (455dclp, Chroma, Bellows Falls, VT).

To image calcium activity in neurons with jRCaMP1b, we used a 595-nm LED (M595L4, Thorlabs, Newton, NJ) with an intensity of 0.5 mW/mm^2 at the sample plane, 585/11-nm excitation filter (FF01-585/11, Semrock, Rochester, NY), and 641/75-nm emission filter (FF02-641/75, Semrock, Rochester, NY). This excitation light joined with the 450-nm photostimulation light at a 593-nm long-pass dichroic (FF593-Di03-25×36, Semrock, Rochester, NY).

To measure the activation spectra of ChroME-mScarlet and our FRET-opsin variants, we constructed a custom monochromator to deliver light ranging from 455 nm to 580 nm at intensities ≥0.1 mW/mm^2 with ∼14 nm of bandwidth (Fig. S1). We focused a high-power white LED (SOLIS-3C, Thorlabs, Newton, NJ) onto a slit and collimated the light that passed through onto a blazed diffraction grating (GR25-0605, Thorlabs, Newton, NJ). This grating was mounted on a motorized, rotating stage (CR1-Z7, Thorlabs, Newton, NJ) that horizontally translated the first-order refracted light. This order then traversed a distance of ∼28″ before passing through a second aperture that selected different wavelength components of the refracted light; the width of this slit also tuned the width of the excitation light spectrum. Finally, we used an $f = 50$ mm lens (LA1131, Thorlabs, Newton, NJ) to refocus the selected portion of the spectrum into a liquid light guide (LLG05-4H, Thorlabs, Newton, NJ). At the output of the liquid light guide, we re-collimated the excitation light with a 25-mm aspheric condenser lens (ACL2520U, Thorlabs, Newton, NJ) and coupled the light into the excitation port of the microscope. We measured the spectral resolution of the monochromator with a miniature spectrometer (FLAME-S-VIS-NIR-ES, OceanOptics, Orlando, FL) and measured the intensity of the output light at each wavelength with a power meter (PM100D, Thorlabs, Newton, NJ).

Data analysis

All photocurrent data analysis was performed using custom MATLAB scripts. Briefly, we isolated the photocurrent driven by individual pulses in each cell and used the average peak as the peak photocurrent for each cell to account for electronic noise introduced by the digitizer. For spectral measurements, all photocurrent responses were recorded using 0.1-mW/mm^2 excitation at each wavelength. To account for the different photon flux at each wavelength under fixed intensity, we applied a scaling factor to each measurement using the equation,

$$I_{corrected}(\lambda) = I_{original}(\lambda) \times \lambda / \lambda_0, \tag{1}$$

where λ_0 was the highest wavelength used, 580 nm. To determine the constructs' off-kinetics, we used least-squares estimation in MATLAB to fit the decay of the photocurrent after 5-ms light pulses to the equation,

$$\text{photocurrent} = A \exp\left(-\frac{t}{\tau}\right) + c, \tag{2}$$

where the A was the current peak amplitude, τ was off-time constant, and c was the constant amplitude. To determine spike probability, we manually inspected traces for all neurons. Spike probability was fit to a sigmoidal function,

$$\text{spike probability} = P_0 + \frac{1 - P_0}{1 + 10^{-\frac{I_{50} - I}{k}}}, \tag{3}$$

where I was the excitation power, P_0 was the fitted spike probability at I = 0 $\mu W/mm^2$, I_{50} was the fitted excitation power to achieve 50% spike probability, and k was the slope of the sigmoid curve.

RESULTS

We developed a rhodopsin-fluorescent protein fusion that increased photocurrent mediated by excitation of a fluorescent protein donor and subsequent FRET to the rhodopsin (Fig. 1 *A*). Our design employed a bright CFP as the donor that could activate current from a paired rhodopsin acceptor. The FRET donor can be maximally excited by blue light with wavelengths ∼50 nm shorter than the rhodopsin acceptor's peak excitation wavelength. The CFP's emission spectrum shares a high overlap with the rhodopsin's activation spectrum. Therefore, by exciting cells expressing this

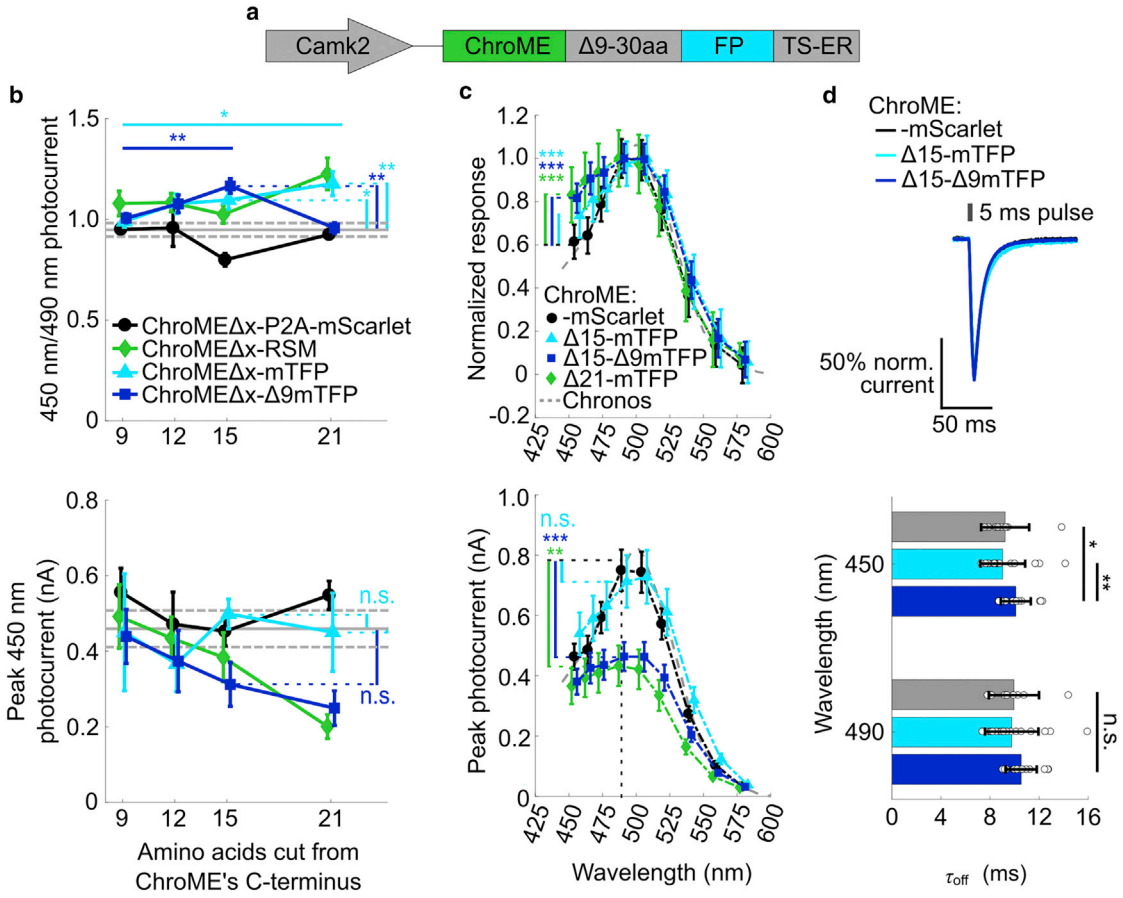

FIGURE 1 FRET between a cyan fluorescent protein and rhodopsin leads to increased photocurrent at short wavelengths. (*a*) All ChroME-CFP variants had 9–30 total amino acids truncated from the region linking ChroME to the fluorescent protein (FP): either Rosmarinus (RSM) or mTFP1. Each construct included a Golgi targeting sequence (TS) and endoplasmic reticulum (ER) export sequence to improve membrane localization. (*b*) Top: the ratio between the peak photocurrent in response to 450-nm excitation and the peak photocurrent in response to 490-nm excitation, all under 100-ms pulses of 0.1 mW/mm^2 light. Key variants had higher photocurrent ratios compared with untagged ChroME. In addition, the 450 nm/490 nm photocurrent ratio significantly increased within each ChroMEΔx-RSM, ChroMEΔx-mTFP, or ChroMEΔx-Δ9mTFP series with increasing truncations of ChroME's C terminus (*$p < 0.05$, **$p < 0.01$, two-sided Wilcoxon rank-sum test, $n \geq 6$ cells per variant). Solid and dashed gray lines represent full-length ChroME's average 450 nm/490 nm photocurrent ratio ± SEM under identical excitation conditions. Bottom: the peak photocurrent in response to 450-nm light under the same pulse conditions as the top panel. Truncations up to 21 amino acids did not significantly decrease ChroMEΔx-mTFP's or ChroMEΔx-Δ9mTFP's peak photocurrents in response to 450-nm illumination compared with the peak photocurrent of full-length, untagged ChroME ($p > 0.05$ for all comparisons; n.s., not significant, two-sided Wilcoxon rank-sum test, $n \geq 6$ cells per variant). Solid and dashed gray lines represent full-length ChroME's average peak photocurrent ± SEM under identical excitation conditions. In both panels, error bars represent mean ± SEM. (*c*) Top: the photocurrent spectra normalized to the photocurrent at the peak activation wavelength for each construct in response to 5-ms, 0.1 mW/mm^2 pulses centered at each wavelength and scaled for the excitation photon flux at each wavelength (section "materials and methods"). The normalized spectra of FRET-opsin constructs broadened toward wavelengths to the blue side of ChroME's peak absorption wavelength. At 455 nm, the normalized photocurrents of our FRET-opsin constructs were higher than the respective normalized photocurrent for unmodified ChroME (***$p < 10^{-3}$, two-sided Wilcoxon rank-sum test, $n \geq 9$ cells per variant). Bottom: the raw peak photocurrent of the normalized responses shown in the top panel, scaled for excitation photon flux at each wavelength (section "materials and methods"). The photocurrent of FRET-opsin constructs was generally lower than the photocurrent of unmodified ChroME. At 490 nm (*vertical dashed line*), or ChroME's peak excitation wavelength, the photocurrents of constructs with more than 15 amino acids removed between ChroME and mTFP were significantly lower than the photocurrent of unmodified ChroME (**$p < 0.01$, ***$p < 10^{-3}$; n.s., not significant, two-sided Wilcoxon rank-sum test, $n \geq 9$ cells per variant). Error bars represent mean ± SEM. Dashed gray lines represent the excitation spectrum of Chronos, adapted from Klapoetke et al. (8). (*d*) Top: example traces of the photocurrent decay of ChroME-mScarlet (*black*), ChroMEΔ15-mTFP (*cyan*), and ChroMEΔ15-Δ9mTFP (*blue*) in response to a 5-ms pulse of 450 nm, 0.1 mW/mm^2 light. Bottom: the average off-kinetics of all variants excited by 490-nm light were statistically comparable, whereas ChroMEΔ15-Δ9mTFP had slightly slower off-kinetics than other variants when excited by 450-nm excitation (*$p \leq 0.05$, **$p \leq 0.01$; n.s., not significant, two-sided Wilcoxon rank-sum test, $n \geq 8$ cells per variant). Error bars represent mean ± standard deviation; white circles represent individual data points.

construct with blue light corresponding to the CFP's peak excitation wavelength, we can drive photocurrent both through FRET between the CFP and rhodopsin and through weak, direct excitation of the rhodopsin by the off-peak excitation light. We theorized that this mechanism would enable us to enhance the excitation efficiency of the

rhodopsin-CFP fusion at shorter wavelengths, effectively shifting the original rhodopsin's activation spectrum.

The FRET-enhanced photocurrent produced by this mechanism depended on the FRET efficiency between the rhodopsin acceptor and CFP donor: FRET efficiency increases with shorter distances between the two domains, with higher overlap between the donor's emission and the acceptor's excitation spectra, and more alignment between the dipole orientations of the donor and acceptor. To maximize both photocurrent and FRET, we employed two protein engineering strategies. First, we minimized the distance between the complex's two domains without adversely affecting the photocurrent or expression of the rhodopsin or fluorescent protein, respectively. Second, we maximized the overlap between the fluorescent protein donor's emission spectrum and the rhodopsin acceptor's activation spectrum. Based on these design criteria, we screened several families of rhodopsin-fluorescent protein constructs, which comprised the fast, sensitive rhodopsin ChroME, and CFPs whose emission spectra overlapped with ChroME's peak activation wavelength at ~500 nm.

Because maximizing FRET critically depends on minimizing the distance between the FRET donor and acceptor, we first determined the maximum number of amino acids that we could truncate from ChroME's C terminus using ChroME's homology with ChR2. We deduced that ChroME's C terminus had approximately 30 amino acids with no secondary structure that could be removed without adversely affecting ChroME's folding. We next generated a series of variants that truncated 0 to 27 amino acids from ChroME's C terminus. For the remainder of the manuscript, these constructs are referred to as ChroMEΔx, where x was the number of truncated C-terminal amino acids. We first placed each truncated version of ChroME in a bicistronic construct to facilitate co-expression of mScarlet. We transfected HEK293T cells with each of these variants, patch clamped mScarlet-positive cells, and recorded the peak photocurrent elicited by 100-ms pulses of 490-nm light with intensities ranging from 0.05 to 1.6 mW/mm^2. We found that ChroME's peak photocurrent elicited by 1.6-mW/mm^2 pulses remained statistically comparable with C terminus truncations of up to 27 amino acids ($p > 0.1$ for all comparisons, two-sided Wilcoxon rank-sum test, $n \geq 6$ cells for all variants; Fig. S2 *A*). We repeated this characterization on a series of ChroME variants fused directly to mScarlet as controls. Fusion to the red fluorescent mScarlet guaranteed there would be virtually no FRET between the domains, and thus probed just the effect of a fused fluorescent protein on the rhodopsin photocurrent. The peak photocurrent of the ChroME-mScarlet variant with its C terminus truncated by 21 amino acids was significantly lower than that of untruncated ChroME-mScarlet for 100-ms pulses of 490-nm light at 1.6 mW/mm^2 ($p < 0.05$, two-sided Wilcoxon rank-sum test, $n \geq 10$ cells for both variants; Fig. S2 *B*). Fusion constructs comprising ChroME and a fluorescent protein did not express when more than 21 amino acids were truncated from ChroME's C terminus, possibly because the close proximity of the rhodopsin and fluorescent protein precluded each domain from folding properly.

Based on these results, we developed two families of FRET-opsin complexes that employed either RSM (40) or mTFP1 (41) as the fluorescent protein donor. We hypothesized that the high overlap between RSM's and TFP's emission spectra and ChroME's activation spectra would support efficient FRET. We further enhanced FRET for the mTFP1 constructs by generating variants using either the full mTFP protein or mTFP with nine amino acids removed from its N terminus, referred to as -Δ9mTFP. Overall, we tested HEK293T cells expressing families of untagged ChroMEΔx, ChroMEΔx-RSM, ChroMEΔx-mTFP, and ChroMEΔx-Δ9mTFP. Each family comprised the Δ9, Δ12, Δ15, and Δ21 amino acid ChroME variants.

Initially, we screened FRET constructs to evaluate FRET under one-photon excitation. We measured the peak photocurrent elicited by 100-ms pulses of either 450-nm or 490-nm light. The 490-nm light directly excited ChroME near the peak of its activation spectrum and drove maximal photocurrent. In contrast, the 450-nm light not only directly excited the rhodopsin with low efficiency but also excited RSM or mTFP at the peak of their absorption spectra. We predicted that the second FRET pathway would elicit higher photocurrent in FRET-opsin constructs than in ChroME constructs when excited by wavelengths below 490 nm.

We used the ratio of the photocurrent driven at 450 nm to the photocurrent driven at 490 nm as a proxy for FRET: high 450 nm/490 nm photocurrent ratios suggested that FRET enhanced photocurrent at shorter excitation wavelengths. Our screen of linkers found the expected effect: the 450 nm/490 nm photocurrent ratios increased with decreasing linker length (Fig. 1 *B*). We found three FRET variants, ChroMEΔ15-mTFP, ChroMEΔ21-mTFP, and ChroMEΔ15-Δ9mTFP, that had both high 450 nm/490 nm photocurrent ratios under 0.1-mW/mm^2 excitation and high peak photocurrent. The three shorter linker variants' 450 nm/490 nm photocurrent ratios were respectively 1.1 ± 0.05, 1.2 ± 0.06, and 1.2 ± 0.04. These ratios were significantly higher than ChroME's original 450 nm/490 nm photocurrent ratio of 0.9 ± 0.03 (mean ± SEM, $p < 0.02$ for all comparisons with ChroME, two-tailed Wilcoxon rank-sum test, $n \geq 6$ cells for each variant; Fig. 1 *B*, *top*). These variants also had peak photocurrents that were statistically comparable with unmodified ChroME under identical stimulation parameters ($p > 0.1$ for all comparisons, two-sided Wilcoxon rank-sum test, $n \geq 6$ cells for each variant; Fig. 1 *B*, *bottom*). The retention of high peak photocurrent suggested that the short linkers in these constructs did not impair folding or expression.

To characterize the FRET effect of these three variants more fully, we built a monochromator to measure each variant's activation spectrum (section "materials and

methods"). We excited HEK293T cells expressing each variant with 5-ms pulses of light ranging from 455 nm to 580 nm with an average fullwidth at half-maximum of 15 nm and power density of 0.1 mW/mm^2 (Fig. S1). This excitation power was the maximum power density achievable using our monochromator across all wavelengths and is below the effective power density for 50% activation (EPD_{50}) of most rhodopsins (16), suggesting that this intensity was in the linear range of the rhodopsins' response (Fig. S3). Consistent with our initial screen, we found that the normalized activation spectra of our FRET-opsin constructs had a prominent increase in the 455–475-nm wavelength range compared with the non-FRET ChroME construct. The normalized activation spectrum of ChroMEΔ15 fused to either mTFP or Δ9mTFP and the spectrum of ChroMEΔ21-mTFP were significantly higher than ChroME's normalized activation spectrum at 455 nm, 465 nm, and 475 nm ($p < 10^{-3}$; two-sided Wilcoxon rank-sum test; n = 18, 15, 12, and 9 cells for ChroMEΔ15-mTFP, ChroMEΔ15-Δ9mTFP, ChroMEΔ21-mTFP, and ChroME-mScarlet respectively; Fig. 1 *C*, *top*), but were nearly equivalent at longer wavelengths. The broadened activation spectrum also translated to slightly higher photocurrent driven by ChroMEΔ15-mTFP compared with ChroME at wavelengths shorter than 490 nm. However, despite a pronounced elevation in their normalized spectra at short wavelengths, ChroMEΔ21-mTFP's and ChroMEΔ15-Δ9mTFP's peak photocurrents were moderately lower than ChroME's when excited by wavelengths from ChroME's peak wavelength at 490 nm ($p < 0.01$ for both ChroMEΔ21-mTFP and ChroMEΔ15-Δ9mTFP, $p = 0.6$ for ChroMEΔ15-mTFP, two-sided Wilcoxon rank-sum test, $n \geq 9$ cells for each variant; Fig. 1 *C*, *bottom*), as well as wavelengths up to approximately 540 nm. The peak photocurrent of ChroMEΔ21-mTFP was nearly equivalent to, but more variable than, ChroMEΔ15-Δ9mTFP's for all excitation wavelengths ($p > 0.29$ for all comparisons, two-sided Wilcoxon rank-sum test, $n \geq 12$ cells for each variant). This increased variability could be due to poorer and less consistent expression levels of rhodopsin-FP fusion constructs with a larger number of amino acids cut from the rhodopsin. Therefore, we focused the remainder of our analysis on ChroMEΔ15-mTFP and ChroMEΔ15-Δ9mTFP.

Finally, due to FRET's nanosecond timescale, FRET-mediated activation does not notably influence the rhodopsins' millisecond-scale closing kinetics (Fig. 1 *D*). ChroME-mScarlet, ChroMEΔ15-mTFP, and ChroMEΔ15-Δ9mTFP had off-kinetics of $\tau_{off} = 9 \pm 2$ ms, 9 ± 2 ms, and 10 ± 1 ms under 450-nm excitation, respectively, and $\tau_{off} = 10 \pm 2$ ms, 10 ± 2 ms, and 10 ± 1 ms under 490-nm excitation, respectively (mean ± SD, n = 18, 15, and 8 cells for ChroMEΔ15-mTFP, ChroMEΔ15-Δ9mTFP, and ChroME-mScarlet, respectively). Surprisingly, ChroMEΔ15-Δ9mTFP's off-kinetics are slightly slower than both ChroMEΔ15-mTFP and ChroME-mScarlet under 450-nm excitation ($p = 3 \times 10^{-3}$ compared with ChroMEΔ15-mTFP, $p = 0.04$ compared with ChroME-mScarlet, two-sided Wilcoxon rank-sum test, n = 18, 15, and 8 cells for ChroMEΔ15-mTFP, ChroMEΔ15-Δ9mTFP, and ChroME-mScarlet, respectively), but not under 490-nm excitation. ChroMEΔ15-Δ9mTFP's slightly slower kinetics suggest that, in addition to adversely affecting photocurrent response, large truncations could modestly affect channel kinetics on the boundary of significance. The discrepancy between the statistical significance at each wavelength could be due to an outlier ChroMEΔ15-mTFP and -mScarlet cell (Fig. 1 *D*). Importantly, each construct's kinetics under 450-nm excitation is statistically comparable with its kinetics under 490-nm excitation. All other comparisons across variants and excitation wavelengths were statistically comparable ($p > 0.05$ for all comparisons, two-sided Wilcoxon rank-sum test).

This high photocurrent and fast kinetics made our FRET-opsin constructs comparable with existing blue-light-shifted rhodopsins under 450-nm excitation. In response to 100-ms pulses of 450-nm light at 1.5 mW/mm^2, ChroMEΔ15-mTFP had a peak photocurrent of 1020 ± 270 pA and off-kinetics of $\tau_{off} = 10 \pm 1$ ms. This is significantly higher photocurrent, but comparable kinetics, compared with the blue-light-activated rhodopsin CheRiff (7), which had a peak photocurrent of 540 ± 110 pA and off-kinetics of $\tau_{off} = 9 \pm 1$ ms under identical excitation conditions ($p = 10^{-4}$ for photocurrent; $p = 0.9$ for kinetics; two-sided Wilcoxon rank-sum test, mean ± SD, $n \geq 6$ cells per construct; Fig. S4).

Finally, to determine whether the rhodopsin-FP paradigm represented a generalizable strategy for modulating rhodopsins' activation spectra, we paired RSM with a slightly blue-shifted rhodopsin, CoChR (8). We performed a similar characterization on these CoChR-RSM constructs as for ChroMEΔX-mTFP and found several notable distinctions between these constructs' characteristics. First, CoChR's photocurrent was more adversely affected by shorter C-terminal truncations and by direct fusion to RSM than analogous ChroME constructs: CoChRΔ21-P2A-mScarlet and all CoChRΔX-RSM constructs had significantly lower photocurrent than untagged CoChR ($p < 0.05$ for all comparisons, two-sided Wilcoxon rank-sum test, $n \geq 6$ cells per construct; Fig. S5 *A*). Second, due to the relatively low overlap between RSM' emission, which peaks at 482 nm, and CoChR's activation spectrum, which peaks at ~470 nm and has comparable excitation efficiency at 450 nm and 490 nm, we did not observe a statistically significant difference in the constructs' 450 nm/490 nm photocurrent ratio (Fig. S5 *B*). Third, in line with these results, we observed that the raw photocurrents of CoChRΔ0-RSM and CoChRΔ12-RSM were considerably lower than that of untagged CoChR across all wavelengths ($p < 10^{-3}$, two-sided Wilcoxon rank-sum test, $n \geq 8$ cells per construct).

However, to a lesser degree compared with the ChroME-mTFP variants, the CoChR-RSM FRET-opsin constructs' normalized spectra were slightly enhanced at 455 nm compared with CoChR-mScarlet (Fig. S5 *C*). These results suggest that, while the FRET-mediated enhancement of a rhodopsins' normalized spectrum may be potentially generalizable, the relationship between the rhodopsin-FP pair and peak photocurrent amplitude is not straightforward.

Based on the enhanced excitability of ChroMEΔ15-mTFP/Δ9mTFP at shorter wavelengths, we sought to determine whether the broadened spectrum translated to higher excitability of neurons expressing these constructs. We transfected cultured hippocampal rat neurons with ChroMEΔ15-mTFP, ChroMEΔ15-Δ9mTFP, or ChroME-mScarlet and excited them with 5-ms pulses of light ranging from 10 to 100 $\mu W/mm^2$ at either 455 nm or 490 nm, corresponding to mTFP's or ChroME's peak excitation wavelength, respectively. We recorded the spike probability for each excitation wavelength to determine the excitation threshold of neurons expressing each construct. Consistent with our previous results, we found that neurons expressing one of the FRET-opsin constructs had a lower spike threshold than neurons expressing ChroME when excited with 455-nm light (Fig. 2 *A*). The average excitation power to achieve 50% spike probability with 455-nm pulses was 31 ± 5 $\mu W/mm^2$, 46 ± 4 $\mu W/mm^2$, and 60 ± 7 $\mu W/mm^2$ for ChroMEΔ15-mTFP, ChroMEΔ15-Δ9mTFP, and ChroME-mScarlet, respectively (mean ± SEM, n = 10 cells per construct). The excitation power required to drive spikes in ChroMEΔ15-mTFP-expressing neurons was significantly lower than the power required to drive spikes in neurons expressing ChroME-mScarlet ($p = 8 \times 10^{-3}$, two-sided Wilcoxon rank-sum test, n = 10 cells per construct). As expected, we did not observe a decrease in the excitation threshold using 490-nm pulses: ChroMEΔ15-mTFP, ChroMEΔ15-Δ9mTFP, and ChroME-mScarlet had statistically comparable 50% excitation thresholds of 29 ± 4 $\mu W/mm^2$, 43 ± 3 $\mu W/mm^2$, and 32 ± 11 $\mu W/mm^2$ (p = 0.42 or 0.28 for comparisons of ChroMEΔ15-mTFP or ChroMEΔ15-Δ9mTFP with ChroME-mScarlet, respectively; two-sided Wilcoxon rank-sum test, n = 10 cells per construct). These results were consistent with the photocurrent measured in neurons excited by either 455-nm or 490-nm light at 1.5 mW/mm^2 (Fig. 2 *B*): the ratio of photocurrent at 455 nm to photocurrent at 490 nm for neurons expressing ChroMEΔ15-mTFP or ChroMEΔ15-Δ9mTFP was higher than that in neurons expressing ChroME-mScarlet (Fig. 2 *C*, p = 0.01 or 10^{-3} for ChroMEΔ15-mTFP or ChroMEΔ15-Δ9mTFP, respectively, two-sided Wilcoxon rank-sum test, n = 10 cells for

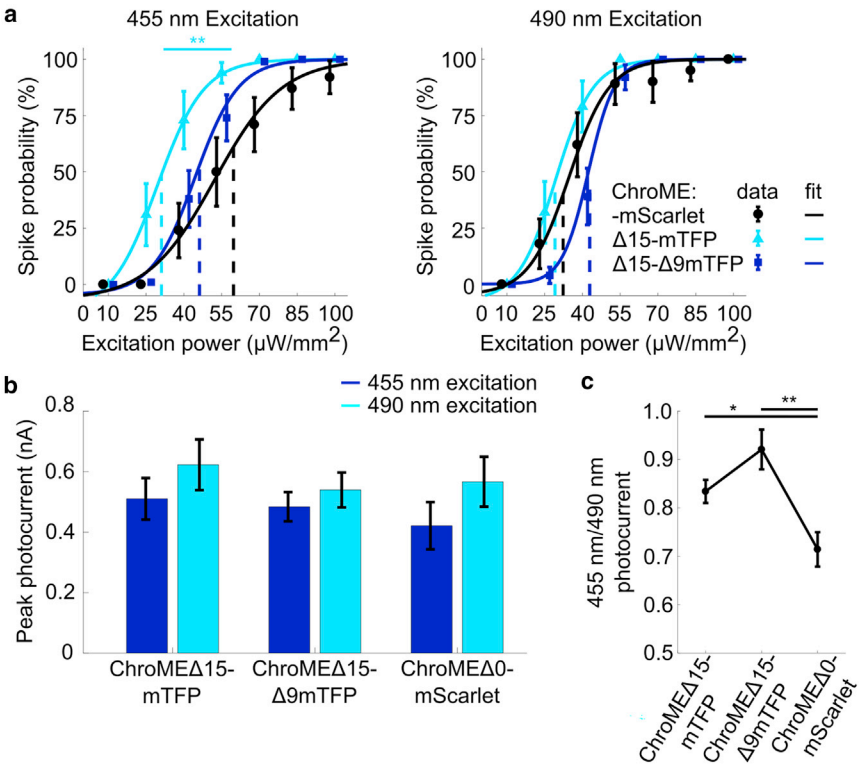

FIGURE 2 FRET enables higher spike probability in neurons at lower excitation powers. (*a*) Left: spike probability as a function of excitation power for 5-ms pulses of 455-nm light. Right: same as left panel, but for 490-nm light. Error bars represent mean ± SEM (n = 10 cells per variant). Solid lines represent spike probabilities fit to a sigmoidal function (section "materials and methods"). Vertical dashed lines correspond to the average excitation power with a 50% spike probability for each variant. The average 50% spike probability threshold under 455-nm excitation for ChroMEΔ15-mTFP was significantly lower than the 50% threshold for ChroME-mScarlet (**p < 0.01, two-sided Wilcoxon rank-sum test, n = 10 cells per variant). (*b*) Peak photocurrent of the neurons whose spike probabilities are shown in (*a*) in response to 5-ms pulses of 0.1 mW/mm^2 light at either 455 nm (*dark blue bars*) or 490 nm (*cyan bars*). Neurons expressing ChroMEΔ15-mTFP and ChroMEΔ15-Δ9mTFP had slightly but not significantly higher photocurrent than ChroME-mScarlet at 455 nm (*dark blue bars*) (p = 0.47 and 0.24 for ChroMEΔ15-mTFP and ChroMEΔ15-Δ9mTFP, respectively, two-sided Wilcoxon rank-sum test, n = 10 cells per variant). Error bars represent mean ± SEM. (*c*) The 455 nm/490 nm photocurrent ratio of the peak photocurrents shown in (*b*). The ratios between the FRET constructs' photocurrent at 455 nm and 490 nm were significantly higher than the same ratio for ChroME-mScarlet (*p < 0.05, **p < 0.01, two-sided Wilcoxon rank-sum test, n = 10 cells per variant). Error bars represent mean ± SEM.

each construct), representing a significant spectral shift. Additionally, this increased excitability was dominantly driven by increased photocurrent under 455-nm excitation rather than decreased photocurrent driven by 490-nm excitation: the photocurrent driven by each wavelength was statistically comparable in cells expressing either ChroMEΔ15-mTFP or ChroME-Δ9mTFP ($p > 0.3$ for both variants, two-sided Wilcoxon rank-sum test, $n = 10$ cells for each construct).

Finally, we sought to determine whether we could use ChroMEΔ15-mTFP in parallel with jRCaMP1b (42) to facilitate dual-channel, simultaneous optogenetic stimulation and calcium imaging. We co-transfected cultured hippocampal rat neurons with two plasmids containing either ChroMEΔ15-mTFP or jRCaMP1b expressed under the CamkIIα promoter (Fig. 3 *A*). However, despite co-expression of the rhodopsin and sensor, we were unable to record crosstalk-free calcium activity in response to blue-light stimulation. This was primarily due to the preservation of ChroMEΔ15-mTFP's moderate response to yellow-light excitation, which was nearly identical in efficiency to that of unmodified ChroME (Fig. 1 *C*). This weak but substantial sensitivity to the continuous, 0.5-mW/mm^2, 585-nm jRCaMP1b imaging light produced a subthreshold ($\sim$5 mV) depolarizing voltage, but, more importantly, prevented neurons from spiking multiple times in repeated trials. Neurons co-expressing ChroMEΔ15-mTFP and jRCaMP1b reliably spiked once per stimulation over the course of five trials when we delivered only blue-light pulses (Fig. 3 *B*). However, repeated blue-light stimulation concurrent with constant yellow imaging light generated wide, low-amplitude action potentials that eventually became suppressed in later trials for single cells (Fig. 3 *C*). On average, neurons that reliably produced a single spike in response to 5-ms, 1.5-mW/mm^2, 450-nm stimuli responded with significantly fewer spikes when stimulated concurrently with constant 585-nm imaging light ($p = 6 \times 10^{-3}$, two-sided Wilcoxon rank-sum test, $n = 10$ cells; Fig. 3 *D*). This depressed excitability could potentially have arisen from desensitization of the rhodopsin to blue-light pulses due to the constant yellow illumination (16,43). This prediction is supported by photocurrent elicited by pulses of 450-nm light in HEK293T cells, which was significantly lower when pulses were delivered under simultaneous yellow-light illumination ($p = 2 \times 10^{-3}$, two-sided Wilcoxon rank-sum test, $n = 6$ cells; Fig. S6). Because pulsed imaging has been used to reduce photocurrent crosstalk in ChroME (11), we employed several imaging LED pulsing parameters while maintaining the same average power per frame as when we used constant 585-nm illumination. In voltage clamped HEK293T cells, we applied identical 450-nm light pulses while pulsing the 585-nm imaging LED at 30 Hz, 90 Hz, or 150 Hz with various intensities and duty cycles. However, due to ChroMEΔ15-mTFP's $\sim$10-ms off-time constant, the crosstalk photocurrent elicited by the imaging light did not decay significantly enough within the time of an imaging frame ($\sim$33 ms) to either decrease the offset in baseline photocurrent or increase the amplitude of 450-nm-elicited

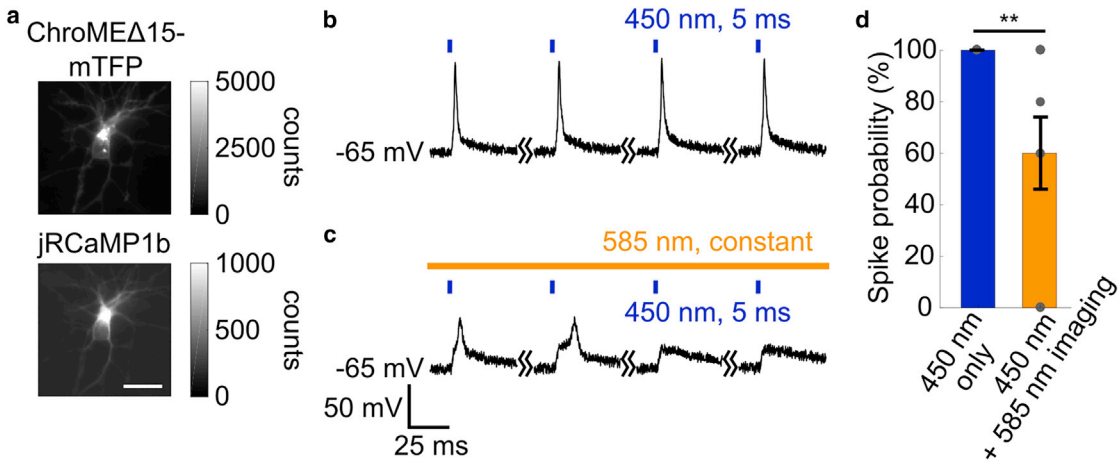

FIGURE 3 ChroME excitation by yellow light prevents simultaneous optogenetics and calcium imaging. (*a*) A neuron co-expressing ChroMEΔ15-mTFP and jRCaMP1b. Top: ChroMEΔ15-mTFP fluorescence in the cyan imaging channel. Bottom: jRCaMP1b expression in the red imaging channel. Scale bar: 20 μm. (*b*) Electrophysiology of a representative ChroMEΔ15-mTFP-expressing neuron under repeated stimulation of 5-ms pulses of 450-nm light at 0.1 mW/mm^2 without 585-nm imaging light. Blue dashes represent the 450-nm stimulation pulses. (*c*) Electrophysiology of the same neuron as in (*b*) under identical 450-nm stimulation conditions delivered simultaneously with constant 585-nm imaging light at 0.5 mW/mm^2. The addition of the imaging light resulted in action potentials with an irregular shape and lower amplitude. Action potentials were also inconsistently evoked by 455-nm pulses of light. Orange bar represents the constant 585-nm imaging light. (*d*) Spike probability of neurons in response to 450-nm stimulation as in (*b*) (*blue bar*) or in response to 450-nm stimulation with 585-nm imaging as in (*c*) (*orange bar*). Illumination of neurons with 450-nm pulses of light concurrently with constant 585-nm imaging light elicited a spike only 60% as frequently as illumination of neurons with 450-nm pulses alone (**$p < 0.01$, two-sided Wilcoxon rank-sum test, $n = 10$ cells). Error bars represent mean $\pm$ SEM.

photocurrent compared with cells under constant 585-nm illumination (Fig. S7).

DISCUSSION

Our work demonstrated that FRET can be used to tune the activation spectra of rhodopsins. By pairing a rhodopsin with the appropriate fluorescent protein and modulating the distance between the domains, we were able to achieve higher activation efficiencies of ChroME using wavelengths up to 50 nm blue-shifted from ChroME's peak activation wavelength. Previous work has demonstrated that photocurrent can be driven in rhodopsins through fusion with a chemiluminescent molecule (30,31) and that spectrally compatible fluorescent tags can contribute secondary peaks to a rhodopsin's activation spectrum (39). Our work further characterized the degree to which the spectrum of a rhodopsin can be modulated through the non-radiative FRET interaction between the rhodopsin and fused fluorescent protein based on both the distance between the domains and spectral compatibility of the FRET domains. This paradigm enabled us to elicit high, temporally precise, light-driven current at blue-shifted wavelengths compared with the unmodified rhodopsin's peak activation wavelength. We screened a suite of rhodopsin-fluorescent protein fusions with an array of truncations to the rhodopsin's C terminus, and we were able to modestly tune the FRET efficiency between the fluorescent protein FRET donor and rhodopsin FRET acceptor. Because FRET is well characterized and predictable, FRET-facilitated excitation represents an alternative strategy to modulate the excitation spectra of optogenetic actuators by optimizing the fusion of a rhodopsin to the appropriate fluorescent protein without directly engineering the rhodopsin's retinal-binding pocket, which has been historically more challenging (17–21). This rational design could bypass time-consuming identifications of new species of rhodopsins with unique spectral sensitivities and screening their photophysical properties.

However, modulating a rhodopsin's activation spectrum via FRET had two main limitations: an imbalanced tradeoff between increased FRET efficiency and decreased photocurrent, and an incomplete spectral shift that resulted in poor compatibility with green-light-activated sensors for dual-channel applications. First, the main method by which we modulated the FRET efficiency of each of our rhodopsin-FP constructs was through decreasing the distance between the domains by truncating amino acids from the C terminus of the rhodopsin or N terminus of the fluorescent protein. However, these truncations introduced an imbalanced tradeoff between FRET efficiency and peak photocurrent. Constructs with shorter truncations, and consequently a greater distance between the rhodopsin and fluorescent protein, had higher raw peak photocurrent but reduced relative enhancement of photocurrent at blue-shifted excitation wavelengths; constructs with longer truncations had a modest increase in blue-light-activation efficiency but significantly lower raw peak photocurrent at the rhodopsin's original peak excitation wavelength. Additionally, we observed decreases in photocurrent in rhodopsin-fluorescent protein fusions at shorter truncations than in the untagged rhodopsin. For example, we observed statistically similar photocurrent in untagged ChroMEΔ27 compared with the control, but we could only cut 21 amino acids from ChroME when it was fused to a fluorescent protein before the construct failed to express.

Second, we were able to broaden the excitation spectrum of ChroME to achieve high-efficiency excitation at blue-shifted wavelengths but did not fully shift the rhodopsin's excitation spectrum. When fused to a CFP, ChroME had excitation efficiency in the 450–480-nm range comparable with ChroME's native excitation efficiency at 500 nm. However, this did not translate to a full shift in the rhodopsin's excitation spectrum; the photocurrent driven by 500–600-nm excitation of ChroMEΔ15-mTFP is virtually equivalent to that driven in the unmodified rhodopsin. The preserved low sensitivity at high wavelengths precludes this tool from crosstalk-free, one-photon excitation experiments in parallel with other green/yellow-light-sensitive tools. This incompatibility is due to the low, sustained photocurrent driven by constant, moderate, yellow-light excitation. Under the same pulse conditions, excitation at wavelengths longer than 580-nm light drives negligible photocurrent. However, when cells expressing ChroMEΔ15-mTFP are excited by 450-nm pulses in conjunction with constant 585-nm illumination, ChroMEΔ15-mTFP's photocurrent changed in two ways: the baseline photocurrent depolarized the cell by a subthreshold but significant voltage, and the peak photocurrent elicited by blue light was suppressed. This suppression could be due to several phenomena, including a decrease in the local ionic gradient necessary to drive photocurrent due to sustained opening of the rhodopsin under yellow-light excitation, desensitization of the rhodopsin to subsequent blue-light pulses after the onset of constant yellow excitation, or inactivation of the rhodopsin's photocycle by red-shifted light (16,24,43–45). This hypothesis is supported by electrophysiology of neurons expressing ChroMEΔ15-mTFP and excited by 2-ms pulses of 450-nm light at 1.5 mW/mm^2 under constant, 585-nm excitation at 0.5 mW/mm^2. In several trials, the blue-light pulses were initially sufficient to drive action potentials but only elicited subthreshold depolarizations after 5 s.

Further engineering of this optogenetic tool or similar tools based on alternative rhodopsins or fluorescent proteins could improve its utility in additional modern neuroscientific experimental paradigms. Additional C-terminal truncations could further improve photocurrent at shorter wavelengths, while the same cuts could simultaneously reduce the native rhodopsin's photocurrent at longer wavelengths. Such an idealistic result could increase our capability to perform crosstalk-free, dual-channel experiments

with these tools, specifically dual-color simultaneous optogenetics and imaging or two-photon optogenetic excitation. Crosstalk-free dual-color optogenetics and imaging could enable genetically targeted, optogenetic excitation of a particular neural population expressing a FRET-opsin in one channel, and imaging of the neural activity of another population expressing a red genetically encoded sensor in another channel. This paradigm would enable neuroscientists to investigate the circuit dynamics between these populations on a large or mesoscopic scale. Enhanced two-photon optogenetic excitation would improve neuroscientists' ability to target single cells at lower laser powers, which could reduce tissue heating or off-target excitation (46). The superior spatial resolution imparted by two-photon optogenetics could enable researchers to investigate the role of individual neurons in driving ensemble activity with high precision (47).

Our current FRET-opsin configuration broadened ChroME's activation spectrum, which could potentially facilitate excitation of the rhodopsin at shorter wavelengths. The effect is modest due to both the modest increase in ChroME's spectrum at shorter wavelengths and relatively narrow absorption spectra of fluorescent proteins compared with rhodopsins. However, several strategies could improve upon the design described here to engineer a rhodopsin-fluorescent protein fusion that is more compatible with a wider range of experimental designs. First, a more comprehensive screen of the linker at the rhodopsin-FP interface or of alternative rhodopsins could potentially overcome our construct's limitations in dual-color experiments. It is possible that screening short linkers between the FRET donor and acceptor or exploring a wider range of linker compositions could result in a more optimal tradeoff than we observed between the enhanced photocurrent at blue-shifted wavelengths and native photocurrent. Short linkers could further increase FRET, which would enhance the blue-light-activated photocurrent's relative contribution to the rhodopsin's activation spectrum. Balanced with reduction in the green- or yellow-light-activated photocurrent arising from truncations to the rhodopsin, this paradigm could effectively produce a narrow, blue-shifted spectrum, rather than a broadened spectrum. Additionally, different linker compositions could improve the orientation alignment between the FRET partners. While not engineered in this study, engineering the dipole orientation factor has previously been accomplished through screens of circular permutations of the fluorescent protein donor, which modulated FRET efficiency by nearly 50% (48,49). Alternative rhodopsins with a similar spectrum to ChroME but more tolerant to C terminus truncations could also potentially improve the performance of this type of tool; such rhodopsins could enable higher FRET between the fluorescent protein and rhodopsin without such severe loss of peak photocurrent. The overall enhanced spectral selectivity would result in reduced photocurrent crosstalk when used in parallel with green- or yellow-light-activated genetically encoded sensors and increase this type of construct's utility in such dual-channel experiments. Second, further characterization of these constructs under two-photon excitation could potentially yield improved tools for two-photon optogenetic targeting of neurons. Several CFPs, including those used in this study, have exceptionally high two-photon absorbance cross sections compared with even the brightest engineered green fluorescent proteins (40). A high absorbance cross section translates to high-efficiency excitation of these fluorescent proteins by two-photon excitation. Because rhodopsins have historically struggled to match their one-photon photocurrent under two-photon excitation, it is possible that FRET-driven photocurrent mediated by fluorescent proteins with high two-photon cross sections combined with off-peak rhodopsin photocurrent could supersede on-peak rhodopsin photocurrent under two-photon excitation alone.

CONCLUSION

In summary, we demonstrated a strategy to extend ChroME's activation spectrum into a range up to 50 nm blue-shifted from its original peak excitation wavelength via FRET. The FRET interaction between mTFP1 and ChroME produced increased excitation efficiencies at blue-shifted wavelengths. We controlled the strength of the FRET interaction by modulating the distance between the domains: more amino acids removed from the C terminus of ChroME or N terminus of mTFP1 translated to a higher relative excitation efficiency at shorter wavelengths. While this approach increased FRET, it also decreased the peak photocurrent at ChroME's original excitation peak at ~500 nm. The FRET enhancement was also present in neurons; under 450-nm excitation, neurons expressing a FRET-opsin required lower excitation powers to drive action potentials than neurons expressing unmodified ChroME. Residual ChroME photocurrent in the green to yellow wavelength range suggests that further engineering is required to make these constructs more applicable for crosstalk-free dual-channel applications.

ETHICAL APPROVAL

All animal work was performed in accordance with the Duke Institutional Animal Care and Use Committee (IACUC) guidelines.

DATA AND CODE AVAILABILITY

Data will be made available from the corresponding author upon reasonable request.

SUPPORTING MATERIAL

Supporting material can be found online at https://doi.org/10.1016/j.bpj.2022.03.024.

AUTHOR CONTRIBUTIONS

Y.G. and C.B. conceived and designed all experiments. C.B. performed the experiments and analyzed the data. C.B. and Y.G. wrote the manuscript.

ACKNOWLEDGMENTS

C.B. was supported by the NIGMS NIH NSRA program (T32GM008555). This research was supported by funding from the NIH New Innovator Program (1DP2-NS111505), the Arnold and Mabel Beckman Foundation, the Brain Research Foundation, the Vallee Foundation, and Alfred P. Sloan Foundation.

REFERENCES

1. Nagel, G., D. Ollig, …, P. Hegemann. 2002. Channelrhodopsin-1: a light-gated proton channel in green algae. *Science.* 296:2395–2398.
2. Nagel, G., T. Szellas, …, E. Bamberg. 2003. Channelrhodopsin-2, a directly light-gated cation-selective membrane channel. *Proc. Natl. Acad. Sci. U S A.* 100:13940–13945.
3. Boyden, E. S., F. Zhang, …, K. Deisseroth. 2005. Millisecond-timescale, genetically targeted optical control of neural activity. *Nat. Neurosci.* 8:1263–1268.
4. Zhang, F., M. Prigge, …, K. Deisseroth. 2008. Red-shifted optogenetic excitation: a tool for fast neural control derived from Volvox carteri. *Nat. Neurosci.* 11:631–633.
5. Prigge, M., F. Schneider, …, P. Hegemann. 2012. Color-tuned channelrhodopsins for multiwavelength optogenetics. *J. Biol. Chem.* 287:31804–31812.
6. Lin, J. Y., P. M. Knutsen, …, R. Y. Tsien. 2013. ReaChR: a red-shifted variant of channelrhodopsin enables deep transcranial optogenetic excitation. *Nat. Neurosci.* 16:1499–1508.
7. Hochbaum, D. R., Y. Zhao, …, A. E. Cohen. 2014. All-optical electrophysiology in mammalian neurons using engineered microbial rhodopsins. *Nat. Methods.* 11:825–833.
8. Klapoetke, N. C., Y. Murata, …, E. S. Boyden. 2014. Independent optical excitation of distinct neural populations. *Nat. Methods.* 11:338–346.
9. Rajasethupathy, P., S. Sankaran, …, K. Deisseroth. 2015. Projections from neocortex mediate top-down control of memory retrieval. *Nature.* 526:653–659.
10. Mager, T., D. Lopez de la Morena, …, E. Bamberg. 2018. High frequency neural spiking and auditory signaling by ultrafast red-shifted optogenetics. *Nat. Commun.* 9:1750.
11. Mardinly, A. R., I. A. Oldenburg, …, H. Adesnik. 2018. Precise multimodal optical control of neural ensemble activity. *Nat. Neurosci.* 21:881–893.
12. Bedbrook, C. N., K. K. Yang, …, F. H. Arnold. 2019. Machine learning-guided channelrhodopsin engineering enables minimally invasive optogenetics. *Nat. Methods.* 16:1176–1184.
13. Arrenberg, A. B., F. Del Bene, and H. Baier. 2009. Optical control of zebrafish behavior with halorhodopsin. *Proc. Natl. Acad. Sci. U S A.* 106:17968–17973.
14. Jennings, J. H., C. K. Kim, …, K. Deisseroth. 2019. Interacting neural ensembles in orbitofrontal cortex for social and feeding behaviour. *Nature.* 565:645–649.
15. Robinson, N. T. M., L. A. L. Descamps, …, M. Hausser. 2020. Targeted activation of hippocampal place cells drives memory-guided spatial behavior. *Cell.* 183:2041–2042.
16. Mattis, J., K. M. Tye, …, K. Deisseroth. 2011. Principles for applying optogenetic tools derived from direct comparative analysis of microbial opsins. *Nat. Methods.* 9:159–172.
17. Kim, S. Y., S. A. Waschuk, …, K. H. Jung. 2008. Screening and characterization of proteorhodopsin color-tuning mutations in Escherichia coli with endogenous retinal synthesis. *Biochim. Biophys. Acta.* 1777:504–513.
18. Engqvist, M. K., R. S. McIsaac, …, F. H. Arnold. 2015. Directed evolution of Gloeobacter violaceus rhodopsin spectral properties. *J. Mol. Biol.* 427:205–220.
19. Kato, H. E., M. Kamiya, …, O. Nureki. 2015. Atomistic design of microbial opsin-based blue-shifted optogenetics tools. *Nat. Commun.* 6:7177.
20. Wietek, J., S. Rodriguez-Rozada, …, J. S. Wiegert. 2017. Anion-conducting channelrhodopsins with tuned spectra and modified kinetics engineered for optogenetic manipulation of behavior. *Sci. Rep.* 7:14957.
21. Oda, K., J. Vierock, …, O. Nureki. 2018. Crystal structure of the red light-activated channelrhodopsin Chrimson. *Nat. Commun.* 9:3949.
22. Marshel, J. H., Y. S. Kim, …, K. Deisseroth. 2019. Cortical layer-specific critical dynamics triggering perception. *Science.* 365:eaaw5202.
23. Tashiro, R., K. Sushmita, …, S. P. Tsunoda. 2021. Specific residues in the cytoplasmic domain modulate photocurrent kinetics of channelrhodopsin from Klebsormidium nitens. *Commun. Biol.* 4:235.
24. Yizhar, O., L. E. Fenno, …, K. Deisseroth. 2011. Neocortical excitation/inhibition balance in information processing and social dysfunction. *Nature.* 477:171–178.
25. Bedbrook, C. N., A. J. Rice, …, F. H. Arnold. 2017. Structure-guided SCHEMA recombination generates diverse chimeric channelrhodopsins. *Proc. Natl. Acad. Sci. U S A.* 114:E2624–E2633.
26. Quirin, S., J. Jackson, …, R. Yuste. 2014. Simultaneous imaging of neural activity in three dimensions. *Front Neural Circuits.* 8:29.
27. Rickgauer, J. P., K. Deisseroth, and D. W. Tank. 2014. Simultaneous cellular-resolution optical perturbation and imaging of place cell firing fields. *Nat. Neurosci.* 17:1816–1824.
28. Packer, A. M., L. E. Russell, …, M. Hausser. 2015. Simultaneous all-optical manipulation and recording of neural circuit activity with cellular resolution *in vivo*. *Nat. Methods.* 12:140–146.
29. Forli, A., M. Pisoni, …, T. Fellin. 2021. Optogenetic strategies for high-efficiency all-optical interrogation using blue-light-sensitive opsins. *Elife.* 10:e63359.
30. Berglund, K., E. Birkner, …, U. Hochgeschwender. 2013. Light-emitting channelrhodopsins for combined optogenetic and chemical-genetic control of neurons. *PLoS One.* 8:e59759.
31. Berglund, K., K. Clissold, …, U. Hochgeschwender. 2016. Luminopsins integrate opto- and chemogenetics by using physical and biological light sources for opsin activation. *Proc. Natl. Acad. Sci. U S A.* 113:E358–E367.
32. Zou, P., Y. Zhao, …, A. E. Cohen. 2014. Bright and fast multicoloured voltage reporters via electrochromic FRET. *Nat. Commun.* 5:4625.
33. Gong, Y., C. Huang, …, M. J. Schnitzer. 2015. High-speed recording of neural spikes in awake mice and flies with a fluorescent voltage sensor. *Science.* 350:1361–1366.
34. Kannan, M., G. Vasan, …, V. A. Pieribone. 2018. Fast, *in vivo* voltage imaging using a red fluorescent indicator. *Nat. Methods.* 15:1108–1116.
35. Abdelfattah, A. S., T. Kawashima, …, E. R. Schreiter. 2019. Bright and photostable chemigenetic indicators for extended *in vivo* voltage imaging. *Science.* 365:699–704.
36. Beck, C., and Y. Gong. 2019. A high-speed, bright, red fluorescent voltage sensor to detect neural activity. *Sci. Rep.* 9:15878.
37. Abdelfattah, A. S., R. Valenti, …, E. R. Schreiter. 2020. A general approach to engineer positive-going eFRET voltage indicators. *Nat. Commun.* 11:3444.
38. Kinjo, T., K. Terai, …, M. Matsuda. 2019. FRET-assisted photoactivation of flavoproteins for *in vivo* two-photon optogenetics. *Nat. Methods.* 16:1029–1036.

39. Govorunova, E. G., O. A. Sineshchekov, …, J. L. Spudich. 2020. RubyACRs, nonalgal anion channelrhodopsins with highly red-shifted absorption. *Proc. Natl. Acad. Sci. U S A.* 117:22833–22840.

40. Molina, R. S., T. M. Tran, …, M. Drobizhev. 2017. Blue-shifted green fluorescent protein homologues are brighter than enhanced green flourescent protein under two-photon excitation. *J. Phys. Chem. Lett.* 8:2548–2554.

41. Ai, H. W., J. N. Henderson, …, R. E. Campbell. 2006. Directed evolution of a monomeric, bright and photostable version of Clavularia cyan fluorescent protein: structural characterization and applications in fluorescence imaging. *Biochem. J.* 400:531–540.

42. Dana, H., B. Mohar, …, D. S. Kim. 2016. Sensitive red protein calcium indicators for imaging neural activity. *Elife.* 5:e12727.

43. Hegemann, P., S. Ehlenbeck, and D. Gradmann. 2005. Multiple photocycles of channelrhodopsin. *Biophys. J.* 89:3911–3918.

44. Berndt, A., O. Yizhar, …, K. Deisseroth. 2009. Bi-stable neural state switches. *Nat. Neurosci.* 12:229–234.

45. Gong, X., D. Mendoza-Halliday, …, G. Feng. 2020. An ultra-sensitive step-function opsin for minimally invasive optogenetic stimulation in mice and macaques. *Neuron.* 107:197.

46. Yang, W., L. Carrillo-Reid, …, R. Yuste. 2018. Simultaneous two-photon imaging and two-photon optogenetics of cortical circuits in three dimensions. *Elife.* 7:e32671.

47. Carrillo-Reid, L., S. Han, …, R. Yuste. 2019. Controlling visually guided behavior by holographic recalling of cortical ensembles. *Cell.* 178:447–457.e5.

48. Thestrup, T., J. Litzlbauer, …, O. Griesbeck. 2014. Optimized ratiometric calcium sensors for functional *in vivo* imaging of neurons and T lymphocytes. *Nat. Methods.* 11:175–182.

49. Zhang, D., E. Redington, and Y. Gong. 2021. Rational engineering of ratiometric calcium sensors with bright green and red fluorescent proteins. *Commun. Biol.* 4:924.